Turbulent erosion of a subducting intrusion in the Western Mediterranean Sea

Giovanni Testa[1], Mathieu Dever[2,3], Mara Freilich[4], Amala Mahadevan[2], T. M. Shaun Johnston[5], Lorenzo Pasculli[1,6], Francesco M. Falcieri[1]

[1] Institute of Marine Sciences, Italian National Research Council (CNR-ISMAR), Venice, Italy.
[2] Woods Hole Oceanographic Institution, Woods Hole, 02543, MA, USA
[3] RBR, Ottawa, Canada
[4] Brown University, Providence, RI, USA
[5] Scripps Institution of Oceanography, University of California, San Diego, La Jolla, CA, USA
[6] Department of Environmental Sciences, Informatics and Statistics, University Ca' Foscari of Venice, Via Torino 155, 30172 Mestre, Italy

Correspondence to: Giovanni Testa (giovanni.testa@ve.ismar.cnr.it)

Abstract. Frontal zones within the Western Alboran Gyre (WAG) are characterized by a density gradient resulting from the convergence of Atlantic and Mediterranean waters. Subduction along isopycnals at the WAG periphery can play a crucial role in upper ocean ventilation and influences its stratification and biogeochemical cycles. In 2019, physical parameters (comprising temperature, salinity, turbulent kinetic energy dissipation rates) and biogeochemical data (oxygen and chlorophyll-a) profiles were collected in transects along the northern edge of the WAG. Several intrusions of subducted water with elevated oxygen, chlorophyll-a and spice anomaly were identified towards the center of the anticyclone. These features had elevated kinetic energy dissipation rates on both their upper and lower boundaries. Analysis of the turbulent fluxes involving heat, salt, oxygen, and chlorophyll-a demonstrated a net flux of physical and biogeochemical properties from the intrusions to the surrounding ocean. Either the turbulent or diffusive convection mixing contributed to the observed dilution of the intrusion. Other factors (e.g., water column density stability, variability of the photic layer depth, and organic matter degradation) likely played a role in these dynamics. Enhanced comprehension of the persistence and extent of these features might lead to an improved quantitative parametrization of relevant physical and biogeochemical properties involved in subduction within the study zone.

1 Introduction

The Mediterranean Sea is characterized by a shallow circulation cell and a complex upper-layer circulation featuring numerous quasi-permanent eddies and fronts (Tanhua et al., 2013; Capó et al., 2019; Barral et al., 2021; Bonaduce et al., 2021; Zarokanellos et al., 2022; Sánchez-Garrido and Nadal, 2022). The main 12 Mediterranean thermal fronts were listed by Belkin and Cornillon (2007), whereas a recent work by Sudre et al. (2023) captured an even more complex scenario. Specifically, frontal zones in the Alboran Sea (Western Mediterranean basin) are characterized by a density gradient resulting from the

convergence of Atlantic and Mediterranean waters (Fedele et al., 2022; Garcia-Jove et al., 2022). The Atlantic jet strongly influences the formation of two large-scale anticyclonic gyres within the Alboran Sea (the Eastern and Western Alboran Gyres, WAG; **Fig. 1A**) with a smaller cyclonic gyre typically situated in between (Brett et al., 2020; Sala et al., 2022; Sánchez-Garrido and Nadal, 2022).

Ocean subduction, defined as the physical transfer of water from the mixed layer into the ocean interior (Williams, 2001), plays a pivotal role in upper-ocean ventilation and stratification. It also exerts a profound influence on biogeochemical cycles, thereby contributing to the export of greenhouse gases and the vertical transport of organic carbon (Omand et al., 2015; Olita et al., 2017; Stukel et al., 2017; Ruiz et al., 2019; Zarokanellos et al., 2022). The vertical component of ocean current velocity is typically much smaller than its horizontal counterparts, but areas characterized by meandering frontal features associated with mesoscale eddies are expected to exhibit elevated subduction rates (van Haren et al., 2006). Indeed, vertical velocities of up to 55 m d^{-1} have been observed in the Western Alboran Sea front (Capó and McWilliams, 2022; Garcia-Jove et al., 2022; Rudnick et al., 2022), and net submesoscale subduction rate has been estimated at 0.3 m day^{-1} (Freilich and Mahadevan, 2021). Mesoscale turbulence contains more energy than submesoscale patterns (Storer et al., 2022), although submesoscale features can generate larger vertical velocities than mesoscale structures within frontal zones (Mahadevan, 2016; Ruiz et al., 2019). The relationship between submesoscale velocity and mixing within the boundary layer has been explored in prior studies under conditions of turbulent thermal wind balance (Crowe and Taylor, 2018; McWilliams, 2021) and symmetric instabilities (Thomas et al., 2013; Bachman et al., 2017; Zhou et al., 2022). However, so far there has been limited research that specifically identifies occurrences of quasi-balanced subsurface vertical velocity and examines how mixing responds to such instances.

Vertical motion at fronts is driven by frontogenesis, instability processes, nonlinear Ekman effects, and filamentogenesis (Klein and Lapeyre, 2009; Mahadevan, 2016; Mahadevan et al., 2020a; McWilliams, 2021; Capó and McWilliams, 2022; Garcia-Jove et al., 2022). Instabilities have also been identified as a key source of turbulence and energy dissipation at oceanic fronts (D'Asaro et al., 2011; Carpenter et al., 2020; McWilliams, 2021). Subsurface intrusions carry physical (temperature and salinity) and biogeochemical properties (oxygen and chlorophyll-a) characteristic of the surface mixed layer along isopycnals and extend downward and laterally. Intrusions are often identified because of the co-occurrence of subsurface maxima in oxygen, particulate organic carbon with anomalous temperature and salinity properties (i.e., spice; Omand et al., 2015). Intermittent intrusions subducting along the outer periphery of mesoscale and submesoscale structures have previously been identified (Johnston et al., 2011; Llort et al., 2018; Chapman et al., 2020; Johnson and Omand, 2021; Chen et al., 2021; Capó and McWilliams, 2022; Freilich et al., 2024). This study measures the turbulent erosion of a subducting intrusion at fronts within the Western Alboran Gyre, a major mesoscale feature in the western Mediterranean Sea with a Rossby number of 0.08. Data were collected in the framework of the Coherent Lagrangian Pathways from the Surface Ocean to Interior (CALYPSO) project onboard the R/V *Pourquois Pas?*, that aimed to examine subduction features in close proximity to the unstable front that developed along the northern edge of the WAG (Mahadevan et al., 2020).

Previous studies have investigated turbulence data collected with microstructure probes in both the surface (Cuypers et al., 2012; Forryan et al., 2012; Vladoiu et al., 2021) and deep (Ferron et al., 2021; van Haren, 2023) regions of the Western Mediterranean Sea. However, this work represents the first comprehensive investigation of turbulence in a context of mesoscale-submesoscale subduction at frontal zones within the WAG. This paper begins with a comprehensive description of water column properties and a turbulence dataset. We then conduct an examination of physical and biogeochemical properties across frontal transects to identify and characterize subducting features. Finally, we calculate the turbulent erosion of a selected intrusion of interest.

2 Material and methods

2.1 Sampling strategy and profile inventory

The study zone is highly dynamic and significantly influenced by the eastward-flowing Atlantic jet that sustains the WAG (Sánchez-Garrido and Nadal, 2022). The jet is characterized by a pronounced frontal zone, exhibiting a density contrast of up to 1.0 kg m^{-3} at its boundaries (Oguz et al., 2014).

We conducted five transects across the salinity front identified through operational modeling and satellite estimations in the northern edge of the WAG between March 28th and April 4th 2019 (**Fig. 1B**). Temperature and salinity conditions in the upper water column were sampled with an Underway Conductivity Temperature Depth (UCTD) profiler, resulting in a total of 136 profiles (mean depth: 231 m). Turbulence data were collected on 43 stations (mean depth: 219 m) during the campaign using a microstructure profiler. With the exception of a single station, all stations featured duplicate microstructure profiles, from which the mean value between these replicates was computed. Furthermore, we used a CTD probe to obtain 22 dissolved oxygen and chlorophyll-a profiles (mean depth: 284 m) concurrently with the microstructure profiles.

2.2. Temperature, salinity and derived variables

Temperature (accuracy: 0.001 °C) and salinity (accuracy: 0.0003 S m^{-1}) data were acquired using a Teledyne RD Instruments UCTD profiler, as detailed by Rudnick and Klinke (2007). The sampling rate is 16 Hz, with the UCTD falling velocity ranging between 1.5 and 3.5 m s^{-1}. The spatial resolution between UCTD cycles was approximately 1 km, given a cruise speed of 3 m s^{-1} knots during recovery. The UCTD downcasts were post-processed for sensor alignment, salinity spikes correction and were binned using a spline interpolation onto a vertical grid of 1 m. A comprehensive description of data post-processing procedures can be found in Dever et al., (2019). Key oceanographic parameters, including Absolute Salinity, Conservative Temperature, Brunt–Väisälä frequency (N^2), density ratio and Turner angle and spice were computed using the Gibbs Sea Water oceanographic toolbox of TEOS-10 (https://www.teos-10.org/pubs/gsw).

N^2 serves as an indicator of water column vertical stability and was determined using equation (1):

$$N^2 = -\frac{g}{\rho_0}\frac{\partial \rho}{\partial z} \quad (1)$$

where g represents gravitational acceleration (9.8 ms^{-2}), ρ_0 is a reference seawater density (1025 kg m^{-3}), and $\partial\rho/\partial z$ denotes the variability of potential density with depth. The density ratio quantifies the vertical contributions of Conservative Temperature and Absolute Salinity to the stability of the water column (following the Thermodynamic Equation of Seawater – 2010; IOC et al., 2010). The Turner angle, as outlined by McDougall et al., (1988), was computed to identify water column conditions, including double diffusivity (thermal diffusivity or salt fingering), stability, and instability regimes. Seawater spice, defined as the temperature and salinity variability along isopycnals, was employed to discern water masses with similar density, but varying temperature and salinity characteristics (McDougall et al., 2021). Spice anomaly was computed with respect to the mean spice profile computed in a temperature-salinity space (McDougall and Krzysik, 2015) and obtained including all spice profiles of the dataset. When computing the mean spice for a given density, we effectively combine specific temperature and salinity values that correspond to that density. The resulting spice anomaly then quantifies the deviation of the water parcel with the same density from the mean temperature-salinity combination, enabling the identification of intrusions. Furthermore, mixed layer depth was determined using a density threshold of 0.03 kg m^{-3} relative to the reference density at 10 m depth, as proposed by de Boyer Montégut et al. (2004). Isopycnal strain, which measures the stretching or compression of isopycnal surfaces, was calculated as the vertical gradient of isopycnal displacement (Pinkel et al., 1991). This displacement is defined as the difference between the actual depth of each isopycnal and its expected depth based on the mean density profile calculated along the entire section.

2.3. Detection of subducting intrusions

Observational evidence of water being subducted from the upper ocean layer to below the mixed layer was observed by leveraging the high spatio-temporal resolution of the underway data collected by the UCTD. The presence of subsurface intrusions in a frontal transect was semi-automatically detected from the vertical profiles, based on subsurface spice and temperature anomalies. The detection algorithm proceeds as follows: I) Compute average spice on isopycnals for the campaign (auto). II) Compute spice anomaly on an isopycnal for each profile phase (auto). III) Detect subsurface anomalies in spice anomaly using a peak-finding algorithm based on peak prominence (auto). IV) Retain anomalies with at least 5 samples (i.e., 1.5 m; auto) and occur coherently over more than 3 consecutive profiles (manual).

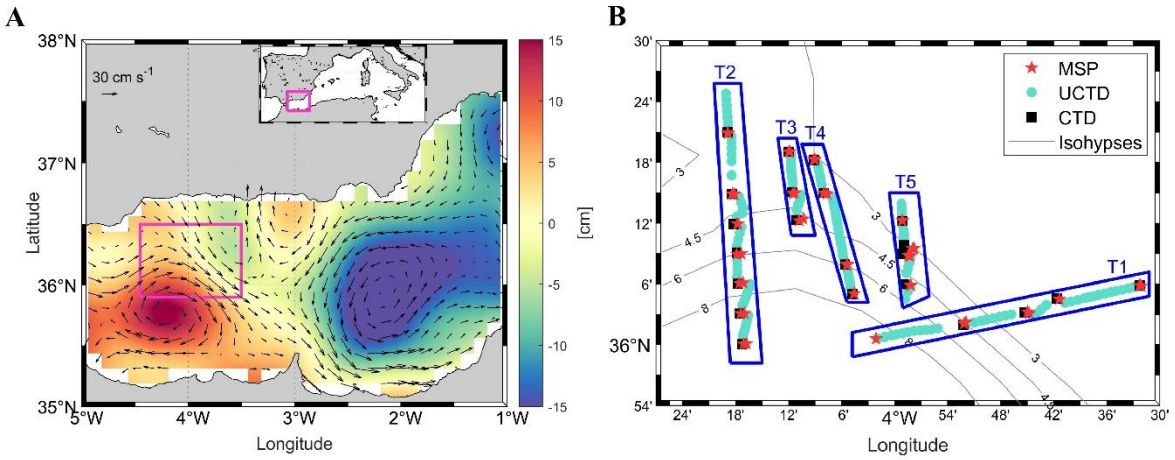

Figure 1. (A) Map of the Alboran Sea showing the mean absolute dynamic topography (colors) and geostrophic currents (arrows) on March 30th-31st, 2019. The purple inset shows the location of the sampling effort, detailed in panel (B), where blue rectangles denote the sampling stations selected for transect (T#) analysis. T1 was realized on March 29th, T2 on March 30th and T3-T5 on March 31st. Isohypses of absolute dynamic topography are depicted as gray lines. Red stars, cyan circles and black squares correspond to sampling stations for the microstructure profiler, underway CTD and CTD, respectively. Daily absolute dynamic topography and geostrophic current data were downloaded from https://data.marine.copernicus.eu/.

2.4. Dissolved oxygen and Chlorophyll-a

We equipped a SeaBird 911plus CTD probe with a SeaBird 43 dissolved oxygen sensor (accuracy: 2% of saturation) and a WET Labs ECO-AFL/FL fluorometer (sensitivity: 0.02 µg l^{-1}) to assess dissolved oxygen and chlorophyll-a concentrations, respectively. The CTD data underwent bin-averaging to achieve a vertical resolution of 0.5 m and was subsequently calibrated using in situ data. Dissolved oxygen estimates were aligned with measurements obtained through Winkler titration (n = 67; Mahadevan et al., 2020b), while chlorophyll-a estimates derived from fluorescence were calibrated against data from fluorometric determinations (n = 140; Alou-Font et al., 2019). A high level of agreement was found between in situ measurements and CTD-derived estimations, as evidenced by coefficient of determination (R^2) values of 0.99 for dissolved oxygen and 0.85 for chlorophyll-a.

Oxygen and chlorophyll-a anomaly on isopycnals were computed following equation (2):

$$X_a = X_\rho - \bar{X}_\rho \quad (2)$$

where X_a represents the variable (i.e., oxygen or chlorophyll-a) anomaly, X_ρ denotes the observed value at a specific density and $\bar{X}_\rho$ is the mean property value corresponding to this density.

2.5. Horizontal ocean currents, Richardson number and potential vorticity

Horizontal current magnitude and direction were collected using a hull-mounted Teledyne RDI Ocean Surveyor Acoustic Doppler Current Profiler (ADCP) operating at a frequency of 150 kHz and with a vertical bin size of 4 m. Detailed post-

processing procedures for ADCP data have been exhaustively documented in Mahadevan et al. (2020b) and Cutolo et al. (2022). Shear squared (S^2) was calculated from ADCP data as the sum of the squares of the vertical gradients of the horizontal velocity components (Gregg, 1989). This value was subsequently used to estimate the Richardson number for shear instabilities (expressed as the ratio between N^2 and S^2; Cushman-Roisin and Beckers, 2011). Ertel potential vorticity (PV) was calculated according to Zhmur et al. (2021) and equation (3):

$$PV = -(f + \zeta)\frac{\partial b}{\partial z} + \left(\frac{\partial v}{\partial z}\frac{\partial b}{\partial x} - \frac{\partial u}{\partial z}\frac{\partial b}{\partial y}\right) \quad (3)$$

where f is the Coriolis parameter, ζ is the relative vorticity, $\partial b/\partial z$ corresponds to the vertical buoyancy gradient, $\partial b/\partial x$ and $\partial b/\partial y$ are the horizontal buoyancy gradients, and u and v represent the horizontal current components.

2.6. Turbulent kinetic energy dissipation rates

Various methods have been employed to quantify turbulent mixing (e.g., integral approaches, finescale parameterizations and direct microstructure measurements; Thorpe, 2005; Shroyer et al., 2018). In this study, we present turbulence dissipation rates observations and derived parameters (Thorpe, 2005) collected using a free-falling microstructure profiler (MSS90D; Sea & Sun Technology). The probe was equipped with two microstructure shear sensors (PNS6; sensitivity: $3.30 \cdot 10^{-4}$ and $3.82 \cdot 10^{-4}$ V m s^2 kg^{-1} at 21 °C), with the final turbulent dissipation rate calculated as the mean of the two shear probe estimates. The profiler's buoyancy was adjusted to achieve a sinking velocity between 0.6 and 0.7 m s^{-1} and the data sampling occurred at a frequency of 1024 Hz but was internally averaged to 512 Hz to comply with signal degradation along the 1.2 km probe cable. Post-processing and turbulent dissipation rate calculations were carried out using the microstructure profiler processing toolbox developed by Schulz et al. (2022). We fine-tuned instrument-specific parameters according to the microstructure profiler employed in this study (e.g., sampling frequency, sensors calibration and sensitivity, distance of other sensors to the shear sensor's tip), while the threshold parameters for data validation from Schulz et al. (2022) were retained. These processing routines were evaluated using two benchmark ATOMIX (Analysing Ocean Turbulence Observations to Quantify Mixing) datasets (Fer et al., 2024), which adhere to best practices for estimating dissipation rates from shear probes (Lueck et al., 2024). The analysis showed strong consistency ($R^2 = 0.98$) between ATOMIX data processed using the Schulz et al. (2022) routines and the Lueck et al. (2024) approach (**Supplementary Fig. 1**), with the former slightly overestimating dissipation rates by a mean of 1.6%.

Kinetic energy dissipation rates (ε) were computed as per equation (4):

$$\varepsilon = \frac{15}{2}\nu\overline{\left(\frac{\partial u}{\partial z}\right)^2} \quad (4)$$

where ν represents the kinematic molecular viscosity and $\overline{(\partial u/\partial z)^2}$ is the spatial average of vertical shear variation with depth (Taylor, 1935). Turbulent dissipation rates from both shear probes were treated separately, averaging all shear spectra within 1 m vertical bin. The shear spectrum results were iteratively fitted to the Nasmyth (Nasmyth, 1970) reference shear spectrum and the deviation of the observed spectrum with respect to the Nasmyth's was used for data quality check. A detailed

description of the data processing procedure was described in Schulz et al. (2022). We performed data-averaging at 1-meter depth intervals, excluding the initial 15 meters of each profile, to mitigate the noise arising from ship motion and wave-breaking (D'Asaro, 2014).

The microstructure data exhibited good agreement (R^2 = 0.89) between the two shear sensors (n=8957; **Supplementary Fig. 2A**), with a stronger correlation observed under elevated turbulence conditions ($\varepsilon > 10^{-7}$ W kg^{-1}) compared to calmer waters ($\varepsilon < 10^{-7}$ W kg^{-1}). Another quality control parameter was the magnitude of the pseudo dissipation rates originated from the profiler high frequency vibrations, consistently one order of magnitude lower than turbulent kinetic energy dissipation rates (**Supplementary Fig. 2B**) and predominantly (36.9%) falling within the range of $1.0 \cdot 10^{-10}$ to $1.6 \cdot 10^{-10}$ W kg^{-1}.

2.7 Turbulent fluxes

Vertical diffusivity (K_z) is computed according to equation (5):

$$K_z = \gamma \frac{\varepsilon}{N^2} \quad (5)$$

where the mixing coefficient is γ = 0.2 (Gregg et al., 2018; Mouriño-Carballido et al., 2021; Lozovatsky et al., 2022), ε is the turbulent kinetic energy dissipation rate and N^2 denotes the squared buoyancy frequency.

We determine turbulent heat (in units of W m^{-2}) and salt fluxes (kg m^{-2} s^{-1}) following Sheehan et al. (2023) and equations (6) and (7):

$$Q_H = -\rho_w C_p K_z \frac{\partial \theta}{\partial z} \quad (6)$$

$$Q_S = 10^{-3}\left(-\rho_w K_z \frac{\partial S}{\partial z}\right) \quad (7)$$

where ρ_w is seawater density, C_p is the specific heat capacity of seawater (3850 J kg^{-1} °C^{-1}), $\partial\theta/\partial z$ corresponds to the vertical gradient of Conservative Temperature, and $\partial S/\partial z$ indicates the vertical gradient of Absolute Salinity. Furthermore, turbulent fluxes of dissolved oxygen and chlorophyll-a (in units of mg m^{-2} s^{-1}) were estimated using equations (8) proposed by Williams et al. (2013):

$$Q_X = -K_z \frac{\partial X}{\partial z} \quad (8)$$

where ∂X denote the variable (i.e., oxygen or chlorophyll-a) vertical gradient with depth.

Our analysis primarily focused on the subducting intrusion identified along transect 2 during the 2019 CALYPSO campaign (**Fig. 1B**). The limited number of microstructure profiles precluded a comprehensive analysis of spatiotemporal intrusions variability along the other transects. To assess the physical and biogeochemical conditions around the subducting intrusion boundaries, we calculated the mean conditions within 5 m inside and outside the intrusion boundaries. The methodology used to calculate diapycnal turbulent fluxes does not account for advective terms involving diapycnal velocity (Du et al., 2017) and assume a constant mixing coefficient (γ) of 0.2. However, γ can vary depending on stratification, turbulence intensity, and water column regimes (Canuto et al., 2011; Gregg et al., 2018). Despite this, variability in γ is typically smaller compared to

variations in turbulence (Le Boyer et al., 2023). It is important to note that the assumption of identical vertical diffusivity for heat, salt, and tracers may introduce potential inaccuracies in flux estimates, which should be considered.

3 Results

3.1 Water column stability and turbulent kinetic energy dissipation rates

High mixing was observed in the surface layer, with localized turbulence peaks in the subsurface water column. Turbulent kinetic energy (TKE) dissipation values displayed considerable variability, with 43.8% of observations falling between $1.3 \cdot 10^{-9}$ and $4.0 \cdot 10^{-9}$ W kg^{-1} (mean ± standard deviation: $8.2 \cdot 10^{-9} \pm 2.4 \cdot 10^{-8}$ W kg^{-1}), with a peak (11.2%) identified in the range of $2.0 \cdot 10^{-9}$ to $2.5 \cdot 10^{-9}$ W kg^{-1}. An analysis of ε probability distribution by depth intervals indicated that 95% of deep ε values were comprised between 10^{-9} and 10^{-7} W kg^{-1} (**Fig. 2A**). In contrast, surface and mid-water depths exhibited a lower proportion (53% and 77%, respectively) within this ε range. Surface waters (<25 m) were characterized by elevated ε values, with 25% and 12% of the data falling within the ranges of 10^{-7}-10^{-6} and 10^{-6}-10^{-5} W kg^{-1}, respectively.

Elevated homogeneity in the shallow water column vertical structure was observed. Indeed, the probability distribution of Brunt–Väisälä frequency (N^2) by depth intervals (**Fig. 2B**) indicated lower stratification in the surface and mid-water layers, where approximately 81% and 67% of values were lower than $0.2 \cdot 10^{-4}$ s^{-2}, respectively. Conversely, the deeper portion (>50 m) of the water column exhibited stronger stratification, with an increased proportion (70%) of N^2 estimations exceeding 0.3 10^{-4} s^{-2}. These patterns were reflected in water column conditions. Examination of Turner angle values revealed a predominantly stable water column, accounting for 74% of the dataset (**Fig. 2C**). However, these stability conditions exhibited notable variations with depth. The shallow layer displayed a more varied scenario with a near-equal distribution between statically unstable and doubly stable conditions. In contrast, the mid-water column featured the highest proportion (27%) of diffusive regimes and the deep layer was primarily characterized (83%) by double stable conditions.

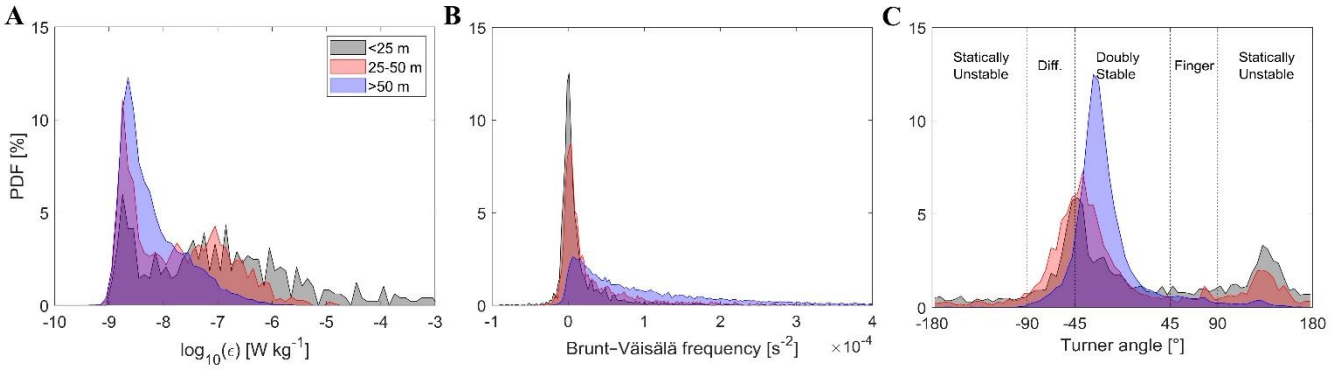

Figure 2. Probability distribution frequency (PDF) by depth intervals for turbulent kinetic energy dissipation rates (A), Brunt–Väisälä frequency (B) and Turner angle values (C). Colored shaded areas in panels correspond to different depth intervals, with gray: 15-25 m; red: 26-50 m; blue: depths >51 m. The names in panel (C) reflect the water column regime according to the Turner angle value (McDougall et al., 1988).

3.2 Transects across the Western Alboran Gyre front

A noticeable depression in the isopycnals was consistently observed in all the transects extending towards the interior of the anticyclone (**Fig. 3** and **Supplementary Fig. 3-7**). The highest ε below the mixed layer was detected adjacent to zones featuring elevated vertical density gradients and deepening along the isopycnals in transects 2 (**Fig. 3**). A deepening of positive spice anomalies from approximately 50 to 100 m was observed at the start of transect 1 and from 15-35 km of transect 2. Subducting intrusions were observed along all transects, except for transect 3, possibly owing to its shorter length (approximately 12 km; **Fig. 3** and **Supplementary Fig. 3-7**). The mean thickness of subducting intrusions was computed at 14.2 m (standard deviation: 9.4 m), ranging from a minimum of 1.7 to a maximum of 42.2 m. The subduction is likely occurring along the frontal direction, following the anticyclonic circulation, rather than necessarily along the tilted isopycnals identified in the transect.

Enhanced ε and diffusivity values were noted in proximity to the base of the mixed layer and in the vicinity of subducting intrusion boundaries (**Fig. 4**). Furthermore, diffusive water column conditions were identified along the upper boundary of the subducting intrusion in transect 2 (**Fig. 3D**) and adjacent to the subducting intrusions within transects 1 and 4. Positive isopycnal strain values were observed at both edges of the subducting intrusion initially, with a predominant concentration of positive values indicating stretching of isopycnal surfaces primarily at the bottom edge as subduction progressed (**Fig. 3E**). The current data along transect 2 illustrated a horizontal velocity magnitude exceeding 60 cm s^{-1} within the interior of the anticyclone, while lower values were observed on its periphery. The subducting intrusion, identified beneath the superficial high-velocity patch and within a zone of elevated shear squared (primarily due to a negative vertical gradient of the zonal velocity component; **Fig. 3F**), was characterized by a horizontal velocity estimated at approximately 0.5 m s^{-1}. The mean Richardson number across the transect was calculated to be 0.89, indicating a generally stable water column with respect to share instabilities. However, lower Richardson numbers were observed in the initial zone of the intrusion (between km 17 and 29 of the transect; **Fig. 3G**). No significant correlation was found between shear and ε, suggesting that stratification may suppress shear-driven turbulence and/or that other sources of turbulence could be influencing the study area. The subducted water exhibited positive potential vorticity (**Fig. 3H**), revealing unfavourable conditions for the generation of symmetric instability.

A deepening of the well oxygenated surface layer towards the center of the anticyclone was observed in transects 1 and 2 (**Supplementary Fig. 3** and **Fig. 3**, respectively). Elevated dissolved oxygen anomaly concentrations (>0.5 mg l^{-1}) were detected inside the subducting intrusion along transect 2 (**Fig. 3I**), with high values deepening from approximately 50 to 120 m. Similarly, anomalous high chlorophyll-a anomaly values were found near the 30 km of transect 2, with anomaly concentrations of up to 1.4 mg m^{-3} detected at a depth of 100 m (**Fig. 3J**).

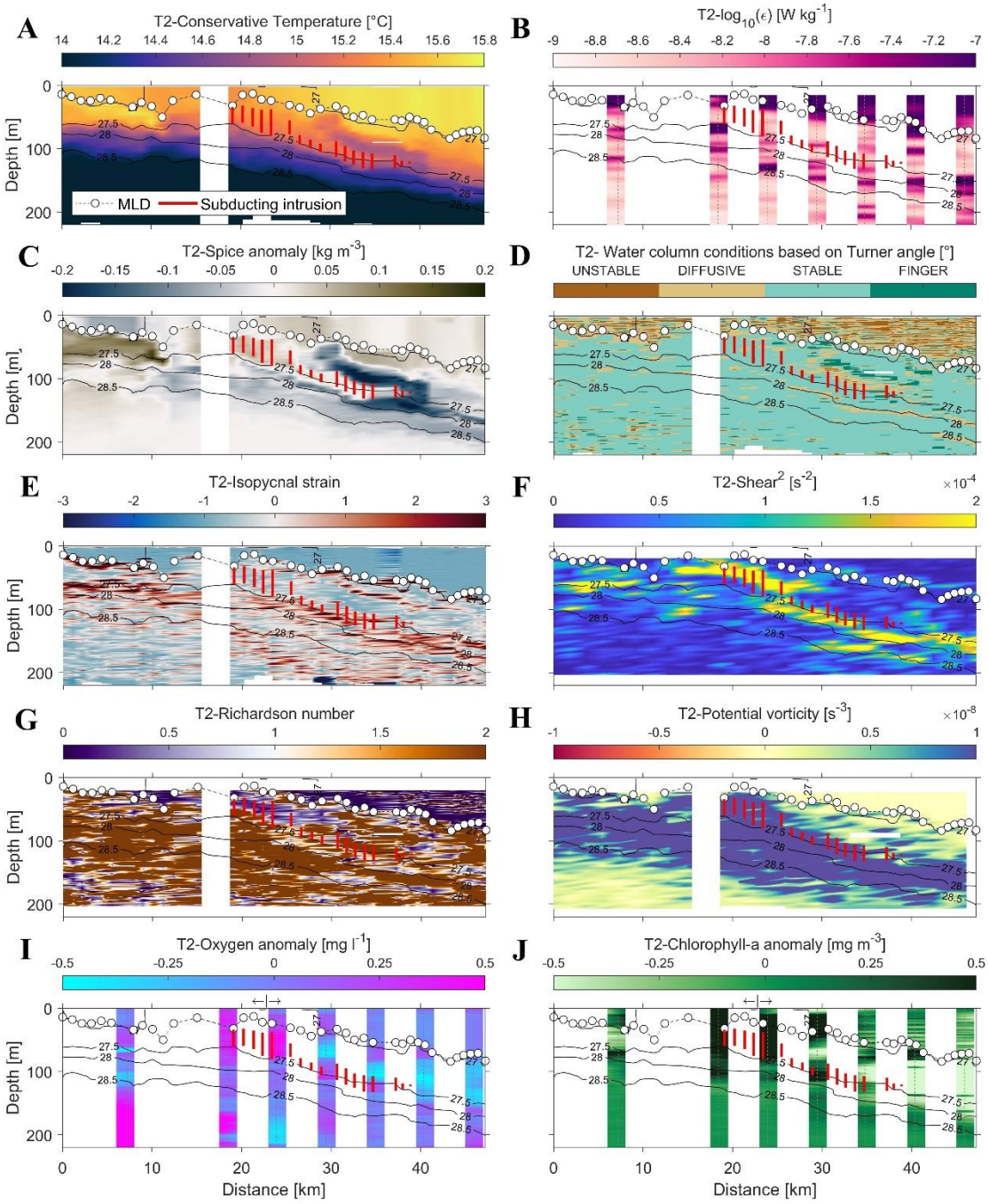

Figure 3. Profiles of Conservative Temperature (A), turbulent kinetic energy dissipation rates (B), spice anomaly (C), water column conditions based on Turner angle estimations (D), isopycnal strain (E), shear squared (F), Richardson number (G), potential vorticity (H), dissolved oxygen anomaly (I), and chlorophyll-a anomaly (J) estimations acquired along transect 2 of the 2019 CALYSPSO campaign. Isopycnals are represented as black lines, while the mixed layer depth and subducting intrusions are denoted by colored points and lines, respectively. The distances between stations were calculated starting from the northernmost sampling point.

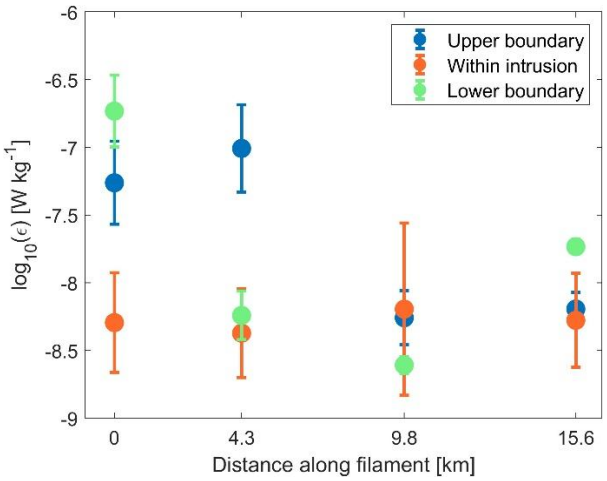

Figure 4. Mean turbulent kinetic energy dissipation values within the intrusion and at its upper and lower boundaries (5 m from the intrusion edges). The errorbars represent the measurement standard deviation.

3.3 Turbulent fluxes around the subducting intrusion

We focused our analysis of the microstructure profiles to transect 2 during the 2019 CALYPSO campaign due to its higher horizontal resolution (**Fig. 1B**). Turbulent fluxes within the interior of the transect 2 intrusion exhibited reduced values compared to water column around both intrusion edges (**Supplementary Fig. 8**). Notably, turbulent fluxes exhibited higher magnitudes within the first two profiles sampling the edges of the subducting intrusion in comparison to the subsequent two profiles (**Fig. 5**). Turbulent fluxes around the intrusion boundaries resulted in a net loss of heat, oxygen and chlorophyll-a properties from within the intrusion to the surrounding ocean, while salinity increased (**Table 1**). Heat, oxygen and chlorophyll-a turbulent fluxes revealed a consistent properties loss at the base of the intrusion towards the deeper layer, while salt fluxes displayed a coherent property loss (gain) at the upper (lower) boundary of the intrusion. Heat loss was consistently recorded near the upper intrusion boundary at all sampling stations, although more variability was observed in oxygen and chlorophyll-a fluxes. The mean absolute values for turbulent fluxes indicated reduced heat, oxygen and chlorophyll-a fluxes near the upper boundary in contrast to the intrusion's base. Specifically, the upper heat flux accounted for only 35% of the magnitude observed near the base of the intrusion, while the upper oxygen and chlorophyll-a fluxes represented 68 and 63%, respectively, of the corresponding bottom flux magnitudes. The fluxes uncertainty was provided in **Supplementary Table 1**.

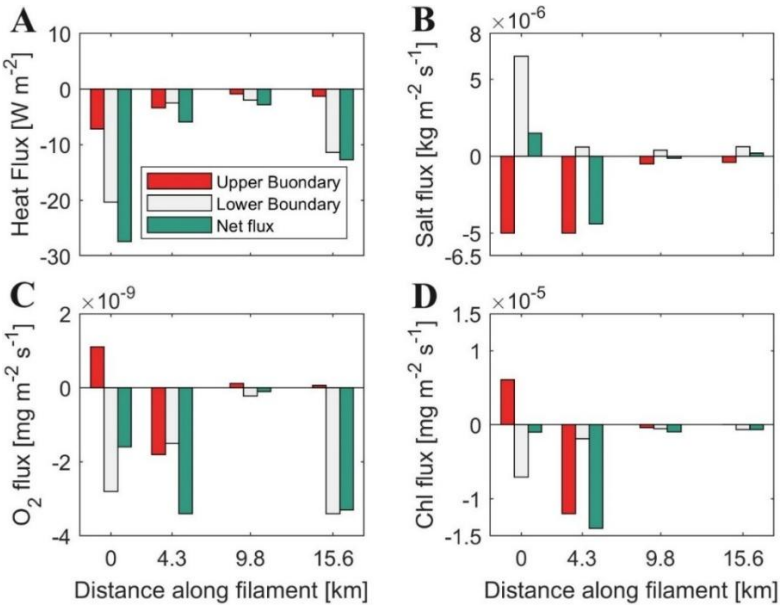

Figure 5. Estimations of turbulent fluxes of heat (A), salt (B), oxygen (C) and chlorophyll-a (D) along the upper and lower boundaries of the subducting intrusion identified within transect T2 of the 2019 CALYPSO campaign and the resulting net flux (in green). The distances between the four stations where the fluxes were calculated (as shown in Supplementary Figure 8) along the subducting intrusion are provided. Positive (negative) values for the turbulent fluxes represent a gain (loss) of the respective variables within the interior of the intrusion.

Table 1. Mean (± 95% confidence interval) Conservative Temperature, Absolute Salinity, dissolved oxygen and chlorophyll-a conditions within the subducting intrusion identified along transect T2 and estimations of daily turbulent heat, salt, oxygen and chlorophyll-a fluxes. The fluxes were computed as the rate of change of properties [(delta flux) (intrusion width)$^{-1}$]. Negative (positive) values denote a loss (gain) within the interior of the intrusion. The distances between the four stations, the intrusion mean depth and thickness are provided.

Variable	Distance along transect [km]			
	0	**4.3**	**9.8**	**15.6**
Intrusion characteristics				
Depth [m]	47	59	99	120
Thickness [m]	25.9	42.2	13.3	24.9
Mean properties				
Temperature [°C]	15.28 ± 0.05	15.27 ± 0.06	15.16 ± 0.03	14.91 ± 0.06
Salinity [g kg^{-1}]	37.03 ± 0.03	37.04 ± 0.04	37.10 ± 0.03	37.15 ± 0.07
Oxygen [mg l^{-1}]	7.74 ± 0.07	7.84 ± 0.10	7.43 ± 0.05	7.16 ± 0.04
Chlorophyll-a [mg m^{-3}]	1.81 ± 0.12	2.16 ± 0.28	1.38 ± 0.13	0.68 ± 0.02
Daily fluxes				
Heat [°C d^{-1}]	$-2.2\cdot10^{-2}$	$-2.9\cdot10^{-3}$	$-4.4\cdot10^{-3}$	$-1.1\cdot10^{-2}$
Salt [g kg^{-1} d^{-1}]	$5.1\cdot10^{-3}$	$-9.1\cdot10^{-3}$	$-7.6\cdot10^{-4}$	$7.0\cdot10^{-4}$
Oxygen [mg l^{-1} d^{-1}]	$-5.5\cdot10^{-3}$	$-6.9\cdot10^{-3}$	$-6.7\cdot10^{-4}$	$-1.1\cdot10^{-2}$
Chlorophyll-a [mg m^{-3} d^{-1}]	$-3.4\cdot10^{-3}$	$-2.9\cdot10^{-2}$	$-6.2\cdot10^{-3}$	$-2.2\cdot10^{-3}$

4 Discussion

4.1 Turbulent kinetic energy dissipation rates in the Western Alboran Sea

The TKE dissipation rates in our study were (mean: $8.2 \cdot 10^{-9}$ W kg^{-1}) found to be comparable to those reported in previous investigations involving microstructure data in the Mediterranean Sea. For instance, Cuypers et al. (2012) calculated mean TKE dissipation values of approximately 10^{-8} W kg^{-1} below the seasonal pycnocline. Our TKE dissipation estimates unveiled an intermediate turbulent environment, between the Mediterranean energetic and quiescent regions (mean: $5.2 \cdot 10^{-8}$ and $4.7 \cdot 10^{-10}$ W kg^{-1}, respectively; Vladoiu et al., 2021). Interestingly, our findings exhibited a closer resemblance to the TKE dissipation observed west of the Gibraltar Strait, where the mean TKE dissipation was $4 \cdot 10^{-9}$ W kg^{-1} in the ocean interior (Fernández-Castro et al., 2014).

The observed peaks in TKE dissipation rates were predictably situated in shallow ocean regions influenced by wave breaking, in close proximity to the base of mixed layer (Zippel et al., 2022) and near the boundaries of subducting intrusions (**Fig. 3**). However, other peaks were detected at deeper levels and did not appear to correlate with aforementioned factors. Mixing processes in the stratified ocean below the mixed layer are often attributed to vertical shear extending below the MLD, penetrative convection and the breaking of internal waves (MacKinnon et al., 2013). The Western Alboran Sea may be influenced by the eastward propagation of internal waves traveling along isopycnals generated by the interaction of tidal currents with bathymetry at the Gibraltar Strait (Thorpe, 2007; Alpers et al., 2008; Bolado-Penagos et al., 2023). While symmetric instabilities have been identified as effective mechanisms for geostrophic energy dissipation in the ocean interior (Zhou et al., 2022), the positive sign of the potential vorticity associated with subducting water in the study area (**Fig. 3H**) suggests that the conditions required for this process to occur may not be met. Another plausible explanation for the deep TKE dissipation peaks could be provided by dissipation associated with subducting intrusions that may have gone undetected by our methodology. Conducting future surveys with mooring and/or glider deployments to identify internal waves within the study zone could significantly advance our comprehension of their spatiotemporal variability and their role in generating deep turbulence along isopycnals.

4.2 Water column regimes

The convergence of Atlantic and Mediterranean waters in the study zone resulted in a robust stratification of the water column, characterized predominantly by doubly stable conditions. Along isopycnals and at the upper boundary of the subducting intrusion (**Figure 3**), we observed instances of diffusive convection regimes. While diffusive convection is typically associated with thermohaline staircases and is more commonly found at higher latitudes (Kelley et al., 2002; van der Boog et al., 2021), the presence of horizontal variability in temperature and salinity conditions in our study area may lead to the formation of

coherent subducting intrusions associated with double diffusive convection (Kelley et al., 2002; Schmitt, 2009). Freilich and Mahadevan (2021) proposed that the specific pathway of subducting intrusions along isopycnals in the study zone could be generated by a combination of mesoscale (geostrophic) frontogenesis and submesoscale (ageostrophic) dynamics.

The subducting intrusion transports subsurface water column properties into the deeper ocean, undergoing erosion along its pathway through a combination of turbulent and diffusive mixing. This dynamic process results in a modification of its inherent properties.

4.3 Turbulent erosion of the intrusion

The elevated TKE dissipation rates in the surface layer, coupled with an increase in stratification with depth can potentially account for the higher diffusivity and turbulent fluxes observed at the start of the intrusion's subduction compared to stations sampled further along the subduction path. Moreover, physical and biogeochemical properties of the subducted water resembled surface conditions more closely than those of the deep layer, resulting in reduced fluxes along the upper boundary of the intrusion compared to the lower boundary (with the exception of the station located at 4.3 km).

The turbulent erosion of the subducting filament led to an overall decrease in temperature, oxygen and chlorophyll-a content within the filament, while salinity increased (**Table 1**). The slight increment in oxygen and chlorophyll-a concentration observed at the second station within the intrusion may be attributed to either the properties gain detected at the upper boundary of the first station, indicating a supply of biogeochemical properties from the surface layer into the intrusion interior, or in situ phytoplankton production (the photic layer was estimated to be around 60 m deep; **Supplementary Fig. 9**).

However, these diapycnal fluxes were too weak to induce a significant dilution of the intrusion, as daily fluxes were orders of magnitude smaller than the mean property values within the intrusion (**Table 1**). These estimates did not account for double-diffusive mixing fluxes characteristic of thermohaline staircases, as such features are predominant at greater depths in the Western Mediterranean Sea (Onken and Brambilla, 2003; Schroeder et al., 2016; Ferron et al., 2021). Despite of this, the estimates of diffusive convection mixing were negligible compared to the turbulent fluxes. In addition to turbulent and diffusive convection mixing, the water column density stability and isopycnal mixing might contribute to the typical vertical variability in subsurface ocean temperature and salinity. Specifically, isopycnal mixing might act an important role in the observed dilution given its contribution in meso- and submesoscale coherent features (Abernathey et al., 2022). Conversely, the decline in oxygen and chlorophyll-a content with depth can be attributed to the deepening of the photic layer, distance from the atmospheric-ocean boundary layer, and processes such as remineralization, respiration, and grazing. The modification of the typical vertical variability in biogeochemical properties induced by subducting intrusions might have profound impacts on ecosystem dynamics within the study zone.

4.4 Biogeochemical significance of subducting intrusions

The Atlantic Jet, which enters the Mediterranean through the Strait of Gibraltar, coupled with coastal upwelling events, transforms our study area into one of the most productive zones in the Mediterranean despite the Mediterranean Sea's well-

known status as an oligotrophic basin (Reale et al., 2020; Sánchez-Garrido and Nadal, 2022). The outer boundary of the WAG has also been identified as a stirring region where properties of the water column are continually exchanged as they are advected towards the center of the anticyclone (Brett et al., 2020; Sala et al., 2022). Subduction of the intrusion may enhance particulate organic carbon export below the mixed layer, reducing its exposure time to remineralization (Freilich et al., 2024). This process contributes to one of the highest export rates observed in the Mediterranean Sea based on sediment trap and particle size distribution profiles data (Ramondenc et al., 2016). Additionally, the mixing associated with subducting intrusions may facilitate the reorganization of phytoplankton communities, traditionally stratified in the photic layer (Mena et al., 2019) and their proliferation. This is especially significant, as nitrates are nearly depleted in the shallow layer north of the WAG (Oguz et al., 2014; Lazzari et al., 2016; García-Martínez et al., 2018). It has been demonstrated that oceanic fronts might act as aggregation areas for planktonic organisms, becoming important foraging areas for higher trophic layers (Acha et al., 2015). Moreover, the transport of chlorophyll-a towards the center of the WAG could lead to an increase in the biomass of diel vertical migrant zooplankton, which tends to be more abundant in the inner part of the gyre compared to its periphery (Yebra et al., 2018).

5 Conclusions

The Western Alboran Gyre is a dynamical feature characterized by high spatiotemporal variability arising from the convergence of Mediterranean and Atlantic waters. Indeed, the northern edge of the WAG water column exhibited notable spatial variability in both physical and biogeochemical characteristics. Specifically, the inner part of this gyre featured higher temperature, current velocity, oxygen content and chlorophyll-a concentration compared to its periphery. Moreover, there was an observable deepening of enhanced Brunt–Väisälä frequency and turbulent kinetic energy dissipation rates towards the anticyclone's center.

The investigation of spice anomaly spatial variability allowed the identification of several subducting intrusions occurring beneath the mixed layer depth, extending from the gyre's outer region towards its center. High turbulent kinetic energy dissipation rates were evident at both the upper and lower boundaries of these intrusions, complemented by localized peaks at deeper levels. The specific factors contributing to these heightened dissipation rates at deeper levels remain elusive.

The turbulent fluxes of heat, salt, oxygen and chlorophyll-a along the intrusion boundaries revealed a consistent net loss of physical and biogeochemical properties from within the intrusion to the surrounding ocean. From a biogeochemical perspective, the subduction intrusion holds significance as it has the potential to amplify the export of particulate organic carbon below the mixed layer. Additionally, it may contribute to the enhancement of diel vertical migrant zooplankton biomass and facilitate the proliferation of phytoplankton communities. Notably, mixing due to turbulence or diffusive convection contributed little to the observed variation in temperature, salinity, oxygen or chlorophyll-a within the intrusion interior. Other factors, such as water column density stability, variability of the photic layer depth, and organic matter degradation, likely played a role in these dynamics.

While our present study has provided valuable insights into the subduction of intrusions and their turbulent erosion within the Western Alboran Gyre, significant gaps remain in our understanding of the spatiotemporal variability of subducting intrusions. Future targeted surveys that specifically address the persistence and extent of these features might improve quantitative parametrizations of key physical and biogeochemical property subduction. Explorations encompassing a broader surface of the WAG may reveal asymmetries in intrusion subduction between the WAG's edges and offer an estimate of the total subduction occurring within the WAG.

Funding. CALYPSO constitutes a Departmental Research Initiative funded by the U.S. Office of Naval Research. GT was founded by ISMAR-26-2022-VE and ISMAR-18-2023-VE research fellowships. TMSJ was supported by ONR grant N00014-18-1-2416.

Data availability. The dataset used in this study is stored and openly shared via Zenodo (Testa et al., 2025), a multidisciplinary repository maintained by CERN (European Organization for Nuclear Research).

Author contributions. GT: Conceptualization, Methodology, Software, Validation, Formal analysis, Data Curation, Writing - Original Draft, Writing - Review & Editing, Visualization. MD: Methodology, Software, Data Curation, Writing - Original Draft, Writing - Review & Editing, Supervision. MF: Resources, Writing - Review & Editing. AM: Resources, Writing - Review & Editing, Project administration, Funding acquisition. SJ: Resources, Writing - Review & Editing. LP: Resources, Writing - Review & Editing. FF: Conceptualization, Methodology, Software, Data Curation, Writing - Original Draft, Writing - Review & Editing, Supervision, Project administration, Funding acquisition.

Competing interests. The authors declare that they have no conflict of interest.

Acknowledgements. We extend our sincere appreciation to the captains and crews of the R/V *Pourquois Pas?*, as well as the technical and scientific personnel involved in making measurements and providing support. The authors wish to express their gratitude to Leo Middleton engaging in insightful conversations that influenced the development of this article. Furthermore, we would like to acknowledge all the CALYPSO researchers whose constructive comments during CALYPSO's Padua meeting enriched this study. Finally, we thank the editor and reviewers for their valuable assistance, comments, and suggestions.

References

Abernathey, R., Gnanadesikan, A., Pradal, M. A., and Sundermeyer, M. A.: Isopycnal mixing, in: Ocean Mixing: Drivers, Mechanisms and Impacts, edited by: Meredith, M., and Naveira Garabato, A., Elsevier, 215–256, https://doi.org/10.1016/B978-0-12-821512-8.00016-5, 2022.

Acha, E. M., Piola, A., Iribarne, O., and Mianzan, H (Eds.).: Ecological processes at marine fronts: Oases in the ocean, Springer, Berlin, Germany, 68 pp., ISBN 978-3-319-15479-4, 2015.

Alou-Font, M., Carbonero, A., and Allen, J.: NRV Alliance report on delayed mode calibration of chlorophyll data. CALYPSO19 cruise 28-03/10-04/19 V-1.0.0, SOCIB-Biogeochemistry Tech. Rep., 2019.

Alpers, W., Brandt, P., and Rubino, A.: Internal waves generated in the Straits of Gibraltar and Messina: Observations from space, in: Remote Sensing of the European Seas, Springer Netherlands, 319–330, https://doi.org/10.1007/978-1-4020-6772-3_24, 2008.

Bachman, S. D., Fox-Kemper, B., Taylor, J. R., and Thomas, L. N.: Parameterization of frontal symmetric instabilities. I: Theory for resolved fronts, Ocean Model., 109, 72–95, https://doi.org/10.1016/j.ocemod.2016.12.003, 2017.

Barral, Q. B., Zakardjian, B., Dumas, F., Garreau, P., Testor, P., and Beuvier, J.: Characterization of fronts in the Western Mediterranean with a special focus on the North Balearic Front, Prog. Oceanogr., 197, 102636, https://doi.org/10.1016/j.pocean.2021.102636, 2021.

Belkin, I. M., and Cornillon, P. C.: Fronts in the world ocean's Large Marine Ecosystems, In: International Council for the Exploration of the Sea, Annual Science Conference, Helsinki, Finland. CM 2007/D:21, 33 pp., 2007.

Bolado-Penagos, M., Sala, I., Jesús Gomiz-Pascual, J., González, C. J., Izquierdo, A., Álvarez, Ó., Vázquez, Á., Bruno, M., and van Haren, H.: Analysis of internal soliton signals and their eastward propagation in the Alboran Sea: exploring the effect of subinertial forcing and fortnightly variability, Prog. Oceanogr., 217, 103077, https://doi.org/10.1016/j.pocean.2023.103077, 2023.

Bonaduce, A., Cipollone, A., Johannessen, J. A., Staneva, J., Raj, R. P., and Aydogdu, A.: Ocean mesoscale variability: a case study on the Mediterranean sea from a re-analysis perspective, Front. Earth Sci., 9, 816, https://doi.org/10.3389/feart.2021.724879, 2021.

Brett, G. J., Pratt, L. J., Rypina, I. I., and Sánchez-Garrido, J. C.: The western Alboran gyre: An analysis of its properties and its exchange with surrounding water, J. Phys. Oceanogr., 50, 3379–3402, https://doi.org/10.1175/JPO-D-20-0028.1, 2020.

Canuto, V. M., Cheng, Y., and Howard, A. M.: Vertical diffusivities of active and passive tracers, Ocean Model., 36, 198–207, https://doi.org/10.1016/J.OCEMOD.2010.12.002, 2011.

Capó, E. and McWilliams, J. C.: Coherent lagrangian pathways near an east Alboran front, J. Geophys. Res. Ocean., 127, e2021JC018022, https://doi.org/10.1029/2021JC018022, 2022.

Capó, E., Orfila, A., Mason, E., and Ruiz, S.: Energy conversion routes in the western Mediterranean sea estimated from eddy-mean flow interactions, J. Phys. Oceanogr., 49, 247–267, https://doi.org/10.1175/JPO-D-18-0036.1, 2019.

Carpenter, J. R., Rodrigues, A., Schultze, L. K. P., Merckelbach, L. M., Suzuki, N., Baschek, B., and Umlauf, L.: Shear Instability and Turbulence Within a Submesoscale Front Following a Storm, Geophys. Res. Lett., 47, e2020GL090365, https://doi.org/10.1029/2020GL090365, 2020.

Chapman, C. C., Lea, M. A., Meyer, A., Sallée, J. B., and Hindell, M.: Defining Southern Ocean fronts and their influence on biological and physical processes in a changing climate, https://doi.org/10.1038/s41558-020-0705-4, 24 February 2020.

Chen, S., Wells, M. L., Huang, R. X., Xue, H., Xi, J., and Chai, F.: Episodic subduction patches in the western North Pacific identified from BGC-Argo float data, Biogeosciences, 18, 5539–5554, https://doi.org/10.5194/bg-18-5539-2021, 2021.

Crowe, M. N., and Taylor, J. R.: The evolution of a front in turbulent thermal wind balance. Part 1. Theory, J. Fluid Mech., 850, 179–211, https://doi.org/10.1017/jfm.2018.448, 2018.

Cushman-Roisin, B. and Beckers, J.-M.: Introduction to Geophysical Fluid Dynamics: Physical and Numerical Aspects, Academic Press, ISBN: 978-0-12-088759-0, 2011.

Cutolo, E., Pascual, A., Ruiz, S., Shaun Johnston, T. M., Freilich, M., Mahadevan, A., Shcherbina, A., Poulain, P. M., Ozgokmen, T., Centurioni, L. R., Rudnick, D. L., and D'Asaro, E.: Diagnosing Frontal Dynamics From Observations Using a Variational Approach, J. Geophys. Res. Ocean., 127, e2021JC018336, https://doi.org/10.1029/2021JC018336, 2022.

Cuypers, Y., Bouruet-Aubertot, P., and Marec, C.: Characterization of turbulence from a fine-scale parameterization and microstructure measurements in the Mediterranean Sea during the BOUM experiment, Biogeosciences, 9, 3131–3149, https://doi.org/10.5194/bg-9-3131-2012, 2012.

D'Asaro, E. A.: Turbulence in the upper-ocean mixed layer, Ann. Rev. Mar. Sci., 6, 101–115, https://doi.org/10.1146/annurev-marine-010213-135138, 2014.

D'Asaro, E., Lee, C., Rainville, L., Harcourt, R., and Thomas, L.: Enhanced turbulence and energy dissipation at ocean fronts, Science, 332, 318–322, https://doi.org/10.1126/science.1201515, 2011.

de Boyer Montégut, C., Madec, G., Fischer, A. S., Lazar, A., and Iudicone, D.: Mixed layer depth over the global ocean: An examination of profile data and a profile-based climatology, J. Geophys. Res. Ocean., 109, 1–20, https://doi.org/10.1029/2004JC002378, 2004.

Dever, M., Freilich, M., Hodges, B., Farrar, J., Lanagan, T., and Mahadevan, A.: UCTD and ECOCTD observations from the CALYPSO pilot experiment (2018): Cruise and data report. Woods Hole Oceanographic Institution Tech. Rep., WHOI-2019-01, https://doi.org/10.1575/1912/23637, 2019.

Du, C., Liu, Z., Kao, S. J., and Dai, M.: Diapycnal Fluxes of Nutrients in an Oligotrophic Oceanic Regime: The South China Sea, Geophys. Res. Lett., 44, 11, 510-11, 518, https://doi.org/10.1002/2017GL074921, 2017.

Fedele, G., Mauri, E., Notarstefano, G., and Poulain, P. M.: Characterization of the Atlantic Water and Levantine Intermediate Water in the Mediterranean Sea using 20 years of Argo data, Ocean Sci., 18, 129–142, https://doi.org/10.5194/os-18-129-2022, 2022.

Fer, I., Dengler, M., Holtermann, P., Le Boyer, A., and Lueck, R.: ATOMIX benchmark datasets for dissipation rate measurements using shear probes, Sci. Data, 11, 518, https://doi.org/10.1038/s41597-024-03323-y, 2024.

Fernández-Castro, B., Mouriño-Carballido, B., Benítez-Barrios, V. M., Chouciño, P., Fraile-Nuez, E., Graña, R., Piedeleu, M., and Rodríguez-Santana, A.: Microstructure turbulence and diffusivity parameterization in the tropical and subtropical Atlantic, Pacific and Indian Oceans during the Malaspina 2010 expedition, Deep. Res. Part I Oceanogr. Res. Pap., 94, 15–30, https://doi.org/10.1016/j.dsr.2014.08.006, 2014.

Ferron, B., Bouruet-Aubertot, P., Schroeder, K., Bryden, H. L., Cuypers, Y., and Borghini, M.: Contribution of Thermohaline Staircases to Deep Water Mass Modifications in the Western Mediterranean Sea From Microstructure Observations, Front. Mar. Sci., 8, 544, https://doi.org/10.3389/fmars.2021.664509, 2021.

Forryan, A., Allen, J. T., Edhouse, E., Silburn, B., Reeve, K., and Tesi, E.: Turbulent mixing in the eddy transport of Western Mediterranean Intermediate Water to the Alboran Sea, J. Geophys. Res. Ocean., 117, 9008, https://doi.org/10.1029/2012JC008284, 2012.

Freilich, M. A., Poirier, C., Dever, M., Alou-Font, E., Allen, J., Cabornero, A., Sudek, L., Choi, C. J., Ruiz, S., Pascual, A., Farrar, J. T., Johnston, T. M. S., D'Asaro, E., Worden, A. Z., and Mahadevan, A.: 3D-intrusions transport active surface microbial assemblages to the dark ocean, bioRxiv, 121, 2023.09.14.557835, https://doi.org/10.1073/PNAS.2319937121, 2023.

Freilich, M. and Mahadevan, A.: Coherent Pathways for Subduction From the Surface Mixed Layer at Ocean Fronts, J. Geophys. Res. Ocean., 126, e2020JC017042, https://doi.org/10.1029/2020JC017042, 2021.

Garcia-Jove, M., Mourre, B., Zarokanellos, N. D., Lermusiaux, P. F. J., Rudnick, D. L., and Tintoré, J.: Frontal Dynamics in the Alboran Sea: 2. Processes for Vertical Velocities Development, J. Geophys. Res. Ocean., 127, e2021JC017428, https://doi.org/10.1029/2021JC017428, 2022.

García-Martínez, M. del C., Vargas-Yáñez, M., Moya, F., Santiago, R., Muñoz, M., Reul, A., Ramírez, T., and Balbín, R.: Average nutrient and chlorophyll distributions in the western Mediterranean: RADMED project, Oceanologia, 61, 143–169, https://doi.org/10.1016/j.oceano.2018.08.003, 2019.

Gregg, M. C.: Scaling turbulent dissipation in the thermocline, J. Geophys. Res. Ocean., 94, 9686–9698, https://doi.org/10.1029/jc094ic07p09686, 1989.

Gregg, M. C., D'Asaro, E. A., Riley, J. J., and Kunze, E.: Mixing efficiency in the ocean, Ann. Rev. Mar. Sci., 10, 443-473, https://doi.org/10.1146/annurev-marine-121916-063643, 2018.

IOC, SCOR, and IAPSO: The international thermodynamic equation of seawater – 2010: Calculation and use of thermodynamic properties. Intergovernmental Oceanographic Commission, Manuals and Guides, 56, UNESCO, 196 pp., 2010.

Johnson, A. R. and Omand, M. M.: Evolution of a Subducted Carbon-Rich Filament on the Edge of the North Atlantic Gyre, J. Geophys. Res. Ocean., 126, e2020JC016685, https://doi.org/10.1029/2020JC016685, 2021.

519 Johnston, T. M. S., Rudnick, D. L., and Pallàs-Sanz, E.: Elevated mixing at a front, J. Geophys. Res. Ocean., 116, 11033,
520 https://doi.org/10.1029/2011JC007192, 2011.
521 Kelley, D. E., Fernando, H. J. S., Gargett, A. E., Tanny, J., and Özsoy, E.: The diffusive regime of double-diffusive convection,
522 Prog. Oceanogr., 56, 461-481, https://doi.org/10.1016/S0079-6611(03)00026-0, 2003.
523 Klein, P. and Lapeyre, G.: The oceanic vertical pump induced by mesoscale and submesoscale turbulence, Ann. Rev. Mar.
524 Sci., 1, 351-375, https://doi.org/10.1146/annurev.marine.010908.163704, 2009.
525 Lazzari, P., Solidoro, C., Salon, S., and Bolzon, G.: Spatial variability of phosphate and nitrate in the Mediterranean Sea: A
526 modeling approach, Deep. Res. Part I Oceanogr. Res. Pap., 108, 39–52, https://doi.org/10.1016/j.dsr.2015.12.006, 2016.
527 Le Boyer, A., Couto, N., Alford, M. H., Drake, H. F., Bluteau, C. E., Hughes, K. G., Naveira Garabato, A. C., Moulin, A. J.,
528 Peacock, T., Fine, E. C., Mashayek, A., Cimoli, L., Meredith, M. P., Melet, A., Fer, I., Dengler, M., and Stevens, C. L.:
529 Turbulent diapycnal fluxes as a pilot Essential Ocean Variable, Front. Mar. Sci., 10, 1241023,
530 https://doi.org/10.3389/fmars.2023.1241023, 2023.
531 Llort, J., Langlais, C., Matear, R., Moreau, S., Lenton, A., and Strutton, P. G.: Evaluating Southern Ocean Carbon Eddy-Pump
532 From Biogeochemical-Argo Floats, J. Geophys. Res. Ocean., 123, 971–984, https://doi.org/10.1002/2017JC012861, 2018.
533 Lozovatsky, I. D., Fernando, H. J. S., Jinadasa, S. U. P., and Wijesekera, H. W.: Eddy diffusivity in stratified ocean: a case
534 study in Bay of Bengal, Environ. Fluid Mech., 1–13, https://doi.org/10.1007/s10652-022-09872-3, 2022.
535 Lueck, R., Fer, I., Bluteau, C., Dengler, M., Holtermann, P., Inoue, R., LeBoyer, A., Nicholson, S. A., Schulz, K., and Stevens,
536 C.: Best practices recommendations for estimating dissipation rates from shear probes, Front. Mar. Sci., 11, 1334327,
537 https://doi.org/10.3389/fmars.2024.1334327, 2024.
538 MacKinnon, J., St Laurent, L., and Naveira Garabato, A. C.: Diapycnal mixing processes in the ocean interior, in: International
539 Geophysics, vol. 103, Academic Press, 159–183, https://doi.org/10.1016/B978-0-12-391851-2.00007-6, 2013.
540 Mahadevan, A.: The Impact of Submesoscale Physics on Primary Productivity of Plankton, Ann. Rev. Mar. Sci., 8, 161–184,
541 https://doi.org/10.1146/annurev-marine-010814-015912, 2016.
542 Mahadevan, A., Pascual, A., Rudnick, D. L., Ruiz, S., Tintoré, J., and D'Asaro, E.: Coherent pathways for vertical transport
543 from the surface ocean to interior, Bull. Am. Meteorol. Soc., 101, E1996–E2004, https://doi.org/10.1175/BAMS-D-19-
544 0305.1, 2020a.
545 Mahadevan, A., D'Asaro, E. A., Allen, J. T., Almaraz García, P., Alou-Font, E., Aravind, H. M., Balaguer, P., Caballero, I.,
546 Calafat, N., Carbornero, A., Casas, B., Castilla, C., Centurioni, L. R., Conley, M., Cristofano, G., Cutolo, E., Dever, M.,
547 Enrique Navarro, A., Falcieri, F., Freilich, M., Goodwin, E., Graham, R., Guigand, C., Hodges, B. A., Huntley, H.,
548 Johnston, S., Lankhorst, M., Lermusiaux, P. F. J., Lizaran, I., Mirabito, C., Miralles, A., Mourre, B., Navarro, G., Ohmart,
549 M., Ouala, S., Ozgokmen, T. M., Pascual, A., Pou, J. M. H., Poulain, P. M., Ren, A., Rodriguez Tarry, D., Rudnick, D. L.,
550 Rubio, M., Ruiz, S., Rypina, I. I., Tintore, J., Send, U., Shcherbina, A. Y., Torner, M., Salvador-Vieira, G., Wirth, N., and
551 Zarokanellos, N.: CALYPSO 2019 Cruise Report: field campaign in the Mediterranean, Woods Hole Oceanographic
552 Institution, https://doi.org/10.1575/1912/25266, 2020b.

McDougall, T. J., Thorpe, S. A., and Gibson, C. H.: Small-Scale Turbulence and Mixing in the Ocean: A Glossary, in: Small-scale turbulence and mixing in the ocean, vol. 46, edited by: Nihoul, J. C. J. and Jamart, B. M., Elsevier, 3–9, https://doi.org/10.1016/S0422-9894(08)70533-6, 1988.

McDougall, T. and Krzysik, O.: Spiciness, J. Mar. Res., 73, 141-152, https://doi.org/10.1357/002224015816665589, 2015

McDougall, T. J., Barker, P. M., and Stanley, G. J.: Spice Variables and Their Use in Physical Oceanography, J. Geophys. Res. Ocean., 126, e2019JC01593, https://doi.org/10.1029/2019JC015936, 2021.

McWilliams, J. C.: Oceanic Frontogenesis, Ann. Rev. Mar. Sci., 13, 227–253, https://doi.org/10.1146/annurev-marine-032320-120725, 2021.

Mena, C., Reglero, P., Hidalgo, M., Sintes, E., Santiago, R., Martín, M., Moyà, G., and Balbín, R.: Phytoplankton community structure is driven by stratification in the oligotrophic mediterranean sea, Front. Microbiol., 10, 456694, https://doi.org/10.3389/fmicb.2019.01698, 2019.

Mouriño-Carballido, B., Otero Ferrer, J. L., Fernández Castro, B., Marañón, E., Blazquez Maseda, M., Aguiar-González, B., Chouciño, P., Graña, R., Moreira-Coello, V., and Villamaña, M.: Magnitude of nitrate turbulent diffusion in contrasting marine environments, Sci. Rep., 11, 1–16, https://doi.org/10.1038/s41598-021-97731-4, 2021.

Nasmyth, P. W.: Oceanic turbulence, Ph.D. thesis, University of British Columbia, Canada, https://doi.org/10.14288/1.0302459, 1970.

Oguz, T., Macias, D., Garcia-Lafuente, J., Pascual, A., and Tintore, J.: Fueling plankton production by a meandering frontal jet: A case study for the Alboran sea (Western Mediterranean), PLoS One, 9, e111482, https://doi.org/10.1371/journal.pone.0111482, 2014.

Olita, A., Capet, A., Claret, M., Mahadevan, A., Poulain, P. M., Ribotti, A., Ruiz, S., Tintoré, J., Tovar-Sánchez, A., and Pascual, A.: Frontal dynamics boost primary production in the summer stratified Mediterranean sea, Ocean Dyn., 67, 767–782, https://doi.org/10.1007/s10236-017-1058-z, 2017.

Omand, M. M., D'Asaro, E. A., Lee, C. M., Perry, M. J., Briggs, N., Cetinić, I., and Mahadevan, A.: Eddy-driven subduction exports particulate organic carbon from the spring bloom, Science, 348, 222–225, https://doi.org/10.1126/science.1260062, 2015.

Onken, R. and Brambilla, E.: Double diffusion in the Mediterranean Sea: Observation and parameterization of salt finger convection, J. Geophys. Res. Ocean., 108, 8124, https://doi.org/10.1029/2002jc001349, 2003.

Pinkel, R., Sherman, J., Smith, J., and Anderson, S.: Strain: Observations of the Vertical Gradient of Isopycnal Vertical Displacement, J. Phys. Oceanogr., 21, 527–540, https://doi.org/10.1175/1520-0485(1991)021<0527:sootvg>2.0.co;2, 1991.

Ramondenc, S., Madeleine, G., Lombard, F., Santinelli, C., Stemmann, L., Gorsky, G., and Guidi, L.: An initial carbon export assessment in the Mediterranean Sea based on drifting sediment traps and the Underwater Vision Profiler data sets, Deep. Res. Part I Oceanogr. Res. Pap., 117, 107–119, https://doi.org/10.1016/j.dsr.2016.08.015, 2016.

Reale, M., Giorgi, F., Solidoro, C., Di Biagio, V., Di Sante, F., Mariotti, L., Farneti, R., and Sannino, G.: The Regional Earth System Model RegCM-ES: Evaluation of the Mediterranean Climate and Marine Biogeochemistry, J. Adv. Model. Earth Syst., 12, e2019MS001812, https://doi.org/10.1029/2019MS001812, 2020.

Rudnick, D. L. and Klinke, J.: The underway conductivity-temperature-depth instrument, J. Atmos. Ocean. Technol., 24, 1910–1923, https://doi.org/10.1175/JTECH2100.1, 2007.

Rudnick, D. L., Zarokanellos, N. D., and Tint, J.: A Four-Dimensional Survey of the Almeria–Oran Front by Underwater Gliders: Tracers and Circulation, J. Phys. Oceanogr., 52, 225–242, https://doi.org/10.1175/JPO-D-21-0181.1, 2022.

Ruiz, S., Claret, M., Pascual, A., Olita, A., Troupin, C., Capet, A., Tovar-Sánchez, A., Allen, J., Poulain, P. M., Tintoré, J., and Mahadevan, A.: Effects of Oceanic Mesoscale and Submesoscale Frontal Processes on the Vertical Transport of Phytoplankton, J. Geophys. Res. Ocean., 124, 5999–6014, https://doi.org/10.1029/2019JC015034, 2019.

Sala, I., Bolado-Penagos, M., Bartual, A., Bruno, M., García, C. M., López-Urrutia, Á., González-García, C., and Echevarría, F.: A Lagrangian approach to the Atlantic Jet entering the Mediterranean Sea: Physical and biogeochemical characterization, J. Mar. Syst., 226, 103652, https://doi.org/10.1016/j.jmarsys.2021.103652, 2022.

Sánchez-Garrido, J. C. and Nadal, I.: The Alboran Sea circulation and its biological response: A review, Front. Mar. Sci., 9, 933390, https://doi.org/10.3389/fmars.2022.933390, 2022.

Schmitt, R. W.: Double-Diffusive Convection, in: Encyclopedia of Ocean Sciences, Academic Press, 162–170, https://doi.org/10.1016/B978-012374473-9.00604-4, 2009.

Schroeder, K., Chiggiato, J., Bryden, H. L., Borghini, M., and Ben Ismail, S.: Abrupt climate shift in the Western Mediterranean Sea, Sci. Rep., 6, 1–7, https://doi.org/10.1038/srep23009, 2016.

Schulz, K., Mohrholz, V., Fer, I., Janout, M., Hoppmann, M., Schaffer, J., and Koenig, Z.: A full year of turbulence measurements from a drift campaign in the Arctic Ocean 2019–2020, Sci. Data, 9, 1–11, https://doi.org/10.1038/s41597-022-01574-1, 2022.

Sheehan, P. M. F., Damerell, G. M., Leadbitter, P. J., Heywood, K. J., and Hall, R. A.: Turbulent kinetic energy dissipation rate and associated fluxes in the western tropical Atlantic estimated from ocean glider observations, Ocean Sci., 19, 77–92, https://doi.org/10.5194/os-19-77-2023, 2023.

Shroyer, E. L., Nash, J. D., Waterhouse, A. F., and Moum, J. N.: Measuring Ocean Turbulence, in: Observing the Oceans in Real Time, edited by: Venkatesan, R., Tandon, A., D'Asaro, E., and Atmanand, M. A., Springer, Cham, 99–122, https://doi.org/10.1007/978-3-319-66493-4_6, 2018.

Storer, B. A., Buzzicotti, M., Khatri, H., Griffies, S. M., and Aluie, H.: Global energy spectrum of the general oceanic circulation, Nat. Commun., 13, 1–9, https://doi.org/10.1038/s41467-022-33031-3, 2022.

Stukel, M. R., Aluwihare, L. I., Barbeau, K. A., Chekalyuk, A. M., Goericke, R., Miller, A. J., Ohman, M. D., Ruacho, A., Song, H., Stephens, B. M., and Landry, M. R.: Mesoscale ocean fronts enhance carbon export due to gravitational sinking and subduction, Proc. Natl. Acad. Sci. U. S. A., 114, 1252–1257, https://doi.org/10.1073/pnas.1609435114, 2017.

Sudre, F., Hernández-Carrasco, I., Mazoyer, C., Sudre, J., Dewitte, B., Garçon, V., and Rossi, V.: An ocean front dataset for the Mediterranean sea and southwest Indian ocean, Sci. Data, 10, 1–15, https://doi.org/10.1038/s41597-023-02615-z, 2023.

Tanhua, T., Hainbucher, D., Schroeder, K., Cardin, V., Álvarez, M., and Civitarese, G.: The Mediterranean Sea system: A review and an introduction to the special issue, Ocean Sci., 9, 789–803, https://doi.org/10.5194/os-9-789-2013, 2013.

Taylor, G. I.: Statistical theory of turbulence, Proc. R. Soc. London. Ser. A - Math. Phys. Sci., 151, 421–444, https://doi.org/10.1098/rspa.1935.0158, 1935.

Testa, G., Mahadevan, A., Johnston, T. M. S., and Falcieri, F. M.: CTD, UCTD, ADCP, and MSS data collected during the 2019 CALYPSO campaign in the Western Alboran Gyre, Zenodo [data set], https://doi.org/10.5281/zenodo.15021606, 2025.

Thomas, L. N., Taylor, J. R., Ferrari, R., and Joyce, T. M.: Symmetric instability in the Gulf Stream, Deep. Res. Part II Top. Stud. Oceanogr., 91, 96–110, https://doi.org/10.1016/j.dsr2.2013.02.025, 2013.

Thorpe, S. A.: An introduction to ocean turbulence, Cambridge University Press, England, 291 pp., https://doi.org/10.1017/CBO9780511801198, 2007.

Thorpe, S. A.: The turbulent ocean, Cambridge University Press, England, 439 pp., https://doi.org/10.1017/CBO9780511819933, 2005.

van der Boog, C. G., Dijkstra, H. A., Pietrzak, J. D., and Katsman, C. A.: Double-diffusive mixing makes a small contribution to the global ocean circulation, Commun. Earth Environ., 2, 1–9, https://doi.org/10.1038/s43247-021-00113-x, 2021.

van Haren, H.: Sensitive Temperature Probes Detail Different Turbulence Processes in the Deep Mediterranean, Oceanography, 36, https://doi.org/10.5670/OCEANOG.2023.108, 2023.

van Haren, H., Millot, C., and Taupier-Letage, I.: Fast deep sinking in Mediterranean eddies, Geophys. Res. Lett., 33, 4606, https://doi.org/10.1029/2005GL025367, 2006.

Vladoiu, A., Bouruet-Aubertot, P., Cuypers, Y., Ferron, B., Schroeder, K., Borghini, M., and Leizour, S.: Contrasted mixing efficiency in energetic versus quiescent regions: Insights from microstructure measurements in the Western Mediterranean Sea, Prog. Oceanogr., 195, 102594, https://doi.org/10.1016/j.pocean.2021.102594, 2021.

Williams, C., Sharples, J., Green, M., Mahaffey, C., and Rippeth, T.: The maintenance of the subsurface chlorophyll maximum in the stratified western Irish Sea, Limnol. Oceanogr. Fluids Environ., 3, 61–73, https://doi.org/10.1215/21573689-2285100, 2013.

Williams, R. G.: Ocean Subduction, in: Encyclopedia of Ocean Sciences: Second Edition, Academic Press, 156–166, https://doi.org/10.1016/B978-012374473-9.00109-0, 2001.

Yebra, L., Herrera, I., Mercado, J. M., Cortés, D., Gómez-Jakobsen, F., Alonso, A., Sánchez, A., Salles, S., and Valcárcel-Pérez, N.: Zooplankton production and carbon export flux in the western Alboran Sea gyre (SW Mediterranean), Prog. Oceanogr., 167, 64–77, https://doi.org/10.1016/j.pocean.2018.07.009, 2018.

Zarokanellos, N. D., Rudnick, D. L., Garcia-Jove, M., Mourre, B., Ruiz, S., Pascual, A., and Tintoré, J.: Frontal Dynamics in the Alboran Sea: 1. Coherent 3D Pathways at the Almeria-Oran Front Using Underwater Glider Observations, J. Geophys. Res. Ocean., 127, e2021JC017405, https://doi.org/10.1029/2021JC017405, 2022.

Zhmur, V. V., Novoselova, E. V., and Belonenko, T. V.: Potential Vorticity in the Ocean: Ertel and Rossby Approaches with Estimates for the Lofoten Vortex, Izv. - Atmos. Ocean Phys., 57, 632–641, https://doi.org/10.1134/S0001433821050157, 2021.

Zhou, H., Dewar, W., Yang, W., Liu, H., Chen, X., Li, R., Liu, C., and Gopalakrishnan, G.: Observations and modeling of symmetric instability in the ocean interior in the Northwestern Equatorial Pacific, Commun. Earth Environ., 3, 1–11, https://doi.org/10.1038/s43247-022-00362-4, 2022.

Zippel, S. F., Farrar, J. T., Zappa, C. J., and Plueddemann, A. J.: Parsing the Kinetic Energy Budget of the Ocean Surface Mixed Layer, https://doi.org/10.1029/2021GL095920, 28 January 2022.